Ni Single Atom Catalysts for CO₂ Activation

Marie-Mathilde Millet,[†] Gerardo Algara-Siller,[†] Sabine Wrabetz,[†] Aliaksei Mazheika,[‡] Frank Girgsdies,[†] Detre Teschner,[†,§] Friedrich Seitz,[†] Andrey Tarasov,[†] Sergey V. Levchenko,[‡,∥,⊥] Robert Schlögl,[†,§] and Elias Frei*,[†]

[†]Department of Inorganic Chemistry, Fritz-Haber-Institut der Max-Planck-Gesellschaft, Faradayweg 4-6, 14195 Berlin, Germany

[‡]Department of Theory, Fritz-Haber-Institut der Max-Planck-Gesellschaft, Faradayweg 4-6, 14195 Berlin, Germany

[§]Max-Planck-Institut für Chemische Energiekonversion, Abteilung Heterogene Reaktionen, Stiftstr. 34-36, 45470 Mülheim an der Ruhr, Germany

[⊥]Materials Modeling and Development Laboratory, National University of Science and Technology "MISIS", Leninskii av. 4, 119049 Moscow, Russia

[∥]Center for Electrochemical Energy Storage, Skolkovo Institute of Science and Technology, Nobel Street 3, 143026 Moscow, Russia

S Supporting Information

ABSTRACT: We report on the activation of CO₂ on Ni single-atom catalysts. These catalysts were synthesized using a solid solution approach by controlled substitution of 1−10 atom % of Mg²⁺ by Ni²⁺ inside the MgO structure. The Ni atoms are preferentially located on the surface of the MgO and, as predicted by hybrid-functional calculations, favor low-coordinated sites. The isolated Ni atoms are active for CO₂ conversion through the reverse water−gas shift (rWGS) but are unable to conduct its further hydrogenation to CH₄ (or MeOH), for which Ni clusters are needed. The CO formation rates correlate linearly with the concentration of Ni on the surface evidenced by XPS and microcalorimetry. The calculations show that the substitution of Mg atoms by Ni atoms on the surface of the oxide structure reduces the strength of the CO₂ binding at low-coordinated sites and also promotes H₂ dissociation. Astonishingly, the single-atom catalysts stayed stable over 100 h on stream, after which no clusters or particle formation could be detected. Upon catalysis, a surface carbonate adsorbate-layer was formed, of which the decompositions appear to be directly linked to the aggregation of Ni. This study on atomically dispersed Ni species brings new fundamental understanding of Ni active sites for reactions involving CO₂ and clearly evidence the limits of single-atom catalysis for complex reactions.

Ni$_x$Mg$_{1-x}$O
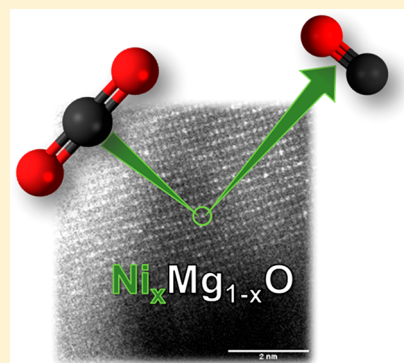
1. INTRODUCTION

Noble metals stabilized on metal oxides are one of the most widely used heterogeneous catalysts also applied in the industry.[1] The size of the metal particles is a cornerstone for the performance of such supported catalysts in terms of metal atom efficiency and selectivity, which both tend to decrease with increasing particle size and broadening size distributions.[2] Hence, there is a need for sophisticated preparation techniques to control with precision the size of those supported metal clusters. Furthermore, the diversity and irregularity of the clusters in size and shape strongly hinder the complete identification of the active site and, as such, the understanding of the reaction. Reducing the complexity of such systems can be achieved by the largest conceivable reduction of both the size and the size distribution of the metal particles by the preparation of "single atom catalysts" (SACs). The first practical synthesis of single atom catalysts was performed by Zhang's group,[2e] achieving the preparation of isolated Pt atoms on an FeOx support. While the denomination of SACs is relatively recent,[2e] the concept of "isolated active site within a

solid catalyst" was introduced much earlier according to Thomas[3] and became prominent thanks to the early work of Grasselli et al.[4] In recent years, many studies were conducted on single atom catalysts, dealing with supported noble metals like Pt,[2e,5] Au,[2d,5a,6] Ir,[7] and Pd[8] but rarely using cheaper and more earth-abundant transition metals.

The understanding of CO₂ activation reactions has become a topic undergoing intense study because of environmental considerations. Among the transition metals efficient for CO₂ activation and hydrogenation reactions, supported Ni catalysts are prominently represented.[9] These catalysts have been extensively studied in methanation[10] and dry reforming of methane[11] reactions. The size of the Ni particles in such systems is known to have a large influence on the selectivity of the methanation reaction.[12] Larger particles lead to more CH₄-selective catalysts, while small particles are more selective toward CO.[13] Recently, Vogt et al. provided some new

mechanistic insights on the CO_2 methanation reaction by correlating the size of the Ni clusters (1−7 nm), to the stability of the reaction intermediates.[14] Interestingly, they observed even for the smallest Ni clusters (~1 nm) the formation of methane. In this study, we go a step further by focusing our interest in the preparation of Ni single atom catalysts, in particular for the hydrogenation of CO_2 to CO or CH_4. To our knowledge, such a challenge has not yet been met successfully, and only a few studies were reported about single Ni atom catalysts, focusing only on electrocatalytic applications or Ni clusters within a single site concept.[11c,15]

Wet chemistry based synthesis methods have been selected for this purpose since, unlike physical deposition synthesis methods like sputtering,[16] they allow the production of larger amounts of catalyst, suitable for their full characterization or even practical industrial applications. One main criterion for the successful synthesis of SACs is to strongly anchor the metal species on the support to avoid their aggregation.[1] To overcome this problem, we used the ability of NiO and MgO to form a solid solution as strategy to prevent the Ni from agglomerating. Both metal oxides crystallize in a face-centered cubic (fcc) structure with almost identical lattice parameters (MgO: 0.4213 nm, NiO: 0.41769 nm).[17] Additionally, MgO is a very suitable support for CO_2 activation reactions since its strong basicity enhances the CO_2 adsorption capacity.[18]

In this study, we report for the first time on the successful synthesis of Ni SACs in the range of 1−10 atom % in the MgO lattice ($Ni_xMg_{1-x}O$). The structure and composition of the precursors and catalysts were thoroughly analyzed with XRD, XPS, XRF, FTIR, STA-MS, microcalorimetry, and electron microscopy. The activity in the rWGS reaction was measured and correlated to the catalyst properties. Additionally, DFT hybrid-functional calculations were performed to better elucidate the role of the Ni atoms with respect to catalytic performance and structural stability. The nature and properties of the active site will be discussed in the context of Ni cluster formation as bridge to the Ni particle based high performance catalysts. Finally, this study addresses the highly important question related to the use of single atom catalyst as models for supported nanoparticle catalysts and to their ability to conduct multielectron redox reactions without limitations.

2. METHODS

2.1. Catalyst Preparation. *Materials.* $Mg(NO_3)_2 \cdot 6H_2O$ (99+%, Acros Organics), $Ni(NO_3)_2 \cdot 6H_2O$ (99+%, Acros Organics), Ammonia 25% (VWR Chemicals, NORMAPUR), and deionized water were obtained from a laboratory purification system.

Synthesis. The $Ni_xMg_{1-x}(OH)_2$ precursors were synthesized by co-precipitation from a Ni and Mg nitrate solution (Σ 1 M) and a 1 M ammonia solution as precipitating agent, in an automated lab reactor. The equimolar mixture was chosen (as opposed to the stoichiometric one) to avoid the formation of $Mg,Ni(NH_3)_n$. While stirring at 300 r·min^{-1}, both solutions were dosed at a rate of 10 g·min^{-1} into deionized water (300 mL) at a controlled temperature of 60 °C. The resulting solution was aged for 1 h before cooled to room temperature. The pH electrode was calibrated at 25 °C with the buffer solutions pH = 7 and pH = 10 (Carl Roth $\pm$0.02). The pH increased strongly with the first drops of ammonia (pH = 9.3) but then remained constant throughout the whole synthesis and aging processes (around pH = 8.8). All parameters of the synthesis were recorded and are shown in the Supporting Information (Figure S1). The slurry was filtrated and the precipitate washed with deionized water until the conductivity was below 0.5 mS·cm^{-1}. The light green solid was dried at 80 °C for 15 h with a heating ramp of 2 °C·min^{-1}

and then calcined in a rotating furnace at 600 °C for 3 h in a flow of 100 mL·min^{-1} consisting of 21% O_2 in argon with a heating ramp of 2 °C·min^{-1}.

2.2. Characterization. *XRD.* The X-ray diffraction (XRD) measurements were performed in Bragg−Brentano geometry on a Bruker AXS D8 Advance II θ/θ diffractometer using Ni-filtered Cu Kα radiation and a position sensitive energy dispersive LynxEye silicon strip detector. The sample powder was filled into the recess of a cup-shaped sample holder, the surface of the powder bed being flush with the sample holder edge (front loading). The powder XRD data were analyzed and the lattice parameters calculated using a full pattern fitting, according to the Rietveld method as implemented in the TOPAS software (TOPAS version 5, copyright 1999−2014 Bruker AXS).

STA-MS. Simultaneous thermoanalysis (TG/DSC) was performed on a Netzsch STA449 Jupiter thermoanalyzer using 10−15 mg of sample placed into an alumina crucible (85 μL) without a lid. Evolution of the gas phase during reaction was monitored with a calibrated quadrupole mass spectrometer (Pfeiffer, QMS200 Omnistar). The thermal decomposition was performed from room temperature to 1000 °C, with a heating ramp of 2 °C·min^{-1} in a 21% O_2 in Ar atmosphere (100 mL·min^{-1}). Experimental mass losses were calculated from 100 to 1000 °C to avoid taking into account the adsorbed surface species (i.e., water).

The specific CO_2 area was calculated using the following formula

$$S_{CO2} = n_s \cdot S \cdot N_A \cdot CSA_{(CO2 \ on \ MgO)} \tag{1}$$

where n_S is the amount of CO_2 molecules, S the stoichiometric factor, N_A the Avogadro number ($6.022140857 \times 10^{23}$), and CSA the cross-sectional area of a CO_2 molecule adsorbed on MgO (22.1×10^{-20} m^2).[19]

Catalytic Testing. The catalytic measurements were performed in a fixed bed flow reactor. A 100 mg portion of the oxidic compound (100−250 μm particle diameter) was loaded into a 6 mm inner diameter stainless steel reactor tube. It was first heated in argon to 350 °C (1 °C·min^{-1}, hold 1 h) to get rid of volatile adsorbed species and then exposed at 200 °C to 100 mL·min^{-1} of a Sabatier gas mixture (72% H_2, 18% CO_2, 10% Ar for balance) at 30 bar pressure. Gas analysis was performed online by a gas chromatograph (Agilent 7890A) equipped with two channels, a thermal conductivity detector was used to analyze CO_2, CO, and argon, while a flame ionization detector was used to analyze MeOH and CH_4 (both of which were combined with different capillary columns: molesieve and plot-Q). All catalytic testings were performed under differential conditions (<3% conversion). Testing with pure silica under the same conditions revealed negligible formation rates at the same order of magnitude as the one of the sample that did not contain any nickel (pure MgO).

Microcalorimetry. Microcalorimetric experiments were carried out in a Calvet calorimeter (SETARAM MS70) combined with custom-designed high vacuum and gas dosing apparatus, which enables the dosage of probe molecules within a range of 0.02 mmol and to calculate the amount of adsorbed molecules. The samples were degassed under UHV at 500 °C for 1 h with a heating ramp of 5 °C·min^{-1}. The pretreatment was conducted in a separate chamber connected to the calorimetric cell. The final pressure in the degassed cell was approximately 10−7 mbar. The cell was cooled to room temperature, placed inside the calorimeter, and connected to the microcalorimetric gas-adsorption system. Subsequently, CO_2 was dosed stepwise at 30 °C. Pressure, adsorption temperature, and heat signals were recorded during all dosing steps.

XPS. All samples were investigated as pressed pellets. XPS spectra were recorded using non-monochromatized Al Kα (1486 eV) excitation and a hemispherical analyzer (Phoibos 150, SPECS). The binding energy (BE) scale was calibrated using a standard Au 4f (7/2) and Cu 2p (3/2) procedure. Charging, in the range of 6−7 eV, was observed with the samples. Binding energy correction for charging was carried out by adjusting the Mg 2p level to 50.3 eV. To calculate the elemental composition, the theoretical cross sections from Yeh and Lindau[20] were used.

TEM. Samples were characterized using a transmission electron microscope JEOL ARM 200F operated at 200 kV. Images were taken with scanning TEM (STEM) and high resolution TEM (HRTEM) modes. The samples were transferred under inert atmosphere without any contact to the ambient.

XRF. X-ray fluorescence spectroscopy (XRF) was performed in a Bruker S4 Pioneer X-ray spectrometer. Sample preparation by melted pellets (100 mg sample with 8.9 g of $Li_2B_4O_7$).

TPR. Temperature-programmed reductions were performed in a fixed bed reactor in a 5% H_2 in argon gas mixture, with a heating rate of 5 °C·min^{-1} (100 mL·min^{-1} for 100 mg catalyst). The H_2 consumption was monitored by a TCD detector. Prior to reduction, the catalysts were heated in argon to 500 °C (5 °C·min^{-1} for 1 h) to get rid of adsorbed surface species. The Ni_10% sample "after catalysis" was taken out of the reactor and set in contact with air before reduction.

BET. Specific surface areas were determined by N_2 physisorption using the BET method[21] in a Quantachrome Autosorb-1 machine. The samples were previously outgassed for 3.5 h at 80 °C.

In Situ IR. The Ni_10% sample was pressed into a self-supporting disk (40.2 mg) and placed in the sample holder in the center of the furnace of the IR cell. The design of the IR cell has been discussed elsewhere.[22] After activation in argon at 500 °C, the reactive gas was introduced in the cell at a flow rate of 120.6 mL·min^{-1} and 10−30 bar pressure to reproduce the reaction conditions of the plug flow catalytic testing. The spectra were recorded with a Varian-670 FTIR spectrometer with a resolution of 2 cm^{-1} and an averaging of 128 scans to achieve satisfactory signal-to-noise ratio. The measurement was performed at 200, 250, and 300 °C after 8 h of time on stream.

CO-Adsorption IR. The low temperature IR measurements were carried out in transmission mode using a PerkinElmer 100 FTIR spectrometer equipped with a pretreatment cell, enabling thermal treatments in controlled atmosphere. Background spectra were obtained by measuring a spectrum of the empty cell at −196 °C. The Ni_10 self-supporting wafers were pretreated once in vacuum to 500 °C and once in an 72% H_2 atmosphere to 300 °C (both with a heating rate of 5 °C·min^{-1} and hold at target temperature for 1 h). The IR cell was then evacuated and cooled to −196 °C for the progressive adsorption of CO (p_{CO} = 0−5 mbar).

2.3. Computational Details. All calculations have been performed using hybrid density functional HSE[23] with ω = 0.11 and fraction of exact exchange α = 0.3, denoted −HSE(0.3). The validation of this method is shown in our previous work.[24] We have used the FHI-aims code,[25] which is all-electron with numerical atomic orbitals. The "tight"[25] numerical settings and basis sets were employed. Relativistic effects were treated within zero-order regular approximation (ZORA).[26] Interatomic interaction at middle and large distances was improved using many-body dispersion correction (MBD).[27] The lattice parameter of cubic MgO was 4.217 Å, as obtained from the bulk calculations with HSE(0.3).

The calculations of adsorption were performed using the slab-periodic model. The k-grids for slabs were set with respect to the 8 × 8 × 8 grid of cubic eight-atomic bulk unit cell. The slab thickness and cell sizes depended on the surface and considered adsorption sites. We used a five-layer slab with a (2 × 2) unit cell for calculations of adsorption on the (001) terrace. For simulations of (001) steps, the four-layer (2 × 3) slab with an additional four-atomic wide semilayer on top was used. The corner position was simulated with a three-layer (3 × 3) slab with 16-atomic square island on top. The (110) surface had eight layers, and the unit cell depended on the coverage and desired Ni surface concentration. The vacuum-gap between slabs was about 200 Å. The adsorption of molecules was considered only on one side of the slab, so the dipole correction was used to prevent unphysical overpolarization. All atoms were allowed to relax with the BFGS algorithm during the search for a minimum on the potential energy surface. The procedure was performed until maximal atomic forces did not exceed 10^{-2} eV/Å.

Adsorption energies were calculated as the difference between total energy of adsorbed system and the sum of total energies of clean surface and gas-phase molecule. We applied the counterpoise method for correction of superposition error.

3. RESULTS AND DISCUSSION

3.1. Structural Analysis of Phase Pure Precursors and Catalysts. Following a co-precipitation recipe (for details see the experimental details), a series of $Ni_xMg_{1−x}O$ samples with varying Ni concentration (0−15 atom %) was synthesized. The samples are named after their Ni concentration; i.e., a sample containing 15 atom % Ni will be named as $Ni\_15(OH)_2$ for the precursor and Ni_15 for the oxidic compound. The XRD patterns of the precursors are illustrated in Figure S2. Rietveld refinement confirmed the phase purity of all samples. Since $Ni(OH)_2$ and $Mg(OH)_2$ have the same crystal structure (brucite type) and close ionic radii, $Ni_xMg_{1−x}(OH)_2$ solid solutions are formed. The evolution of the lattice parameters a and c as a function of the Ni content is shown Figure S3 and Table S1. A linear correlation between both lattice parameters and the Ni loading is observed, confirming the successful incorporation of Ni in the $Mg(OH)_2$ structure as reported in the literature.[28]

All precursors were analyzed using themogravimetry (TG), coupled with simultaneous mass spectrometry (MS). The results are presented in Figure S4. The pure $Mg(OH)_2$ sample shows one characteristic endothermic peak with an onset temperature of 275 °C. With increasing Ni content, this characteristic endothermic peak is shifted to lower onset temperatures. The presence of a single event (as opposed to two distinct ones) gives further evidence of the successful formation of a solid solution, instead of a physical mixture of $Ni(OH)_2$ and $Mg(OH)_2$.[28b] The theoretical and experimental weight losses are summarized in Table S3, and less than 1% deviation is observed. The phase pure character of the precursors is also a prerequisite for the successful solid solution synthesis in the final catalysts.

Figure 1A shows a full pattern Rietveld fit of the calcined Ni_10 sample (XRD patterns of all calcined samples are presented in Figure S5). The fit curve (red line) matches perfectly with the experiment (black line), also confirmed by the flat difference curve (blue line). Figure 1B shows a zoom of the 60−65° region of all diffractograms, exemplarily high-lighting the shift of the 220 reflection to higher 2θ values with increasing Ni content. This corresponds to a continuous decrease of lattice parameter a from 4.217 to 4.208 Å (Figure 1.C). Such behavior is characteristic of the successful incorporation of Ni inside the MgO structure[17a] and a phase pure solid solution sample series. The error bars are invisible, as they are smaller than the size of the symbols used. All of the lattice parameters and their estimated standard deviations are shown Table S2.

3.2. Dispersion. To further confirm the atomic distribution of the Ni atoms in the structure, scanning transmission electron microscopy (STEM) investigations were performed. The high-angle annular dark field (HAADF) STEM image in Figure 2 illustrates the isolated character of the Ni atoms (brighter spots) as part of the MgO lattice (Figure 2B, magnification of 2A, STEM). This was also confirmed by comparison of the dark- and bright-field image shown in Figure S6. Representative for all catalysts, the Ni_10 sample is shown, which has, due to its high Ni loading, a high probability of cluster formation. After extensive analysis of different regions of all the samples, no Ni agglomerates were observed.
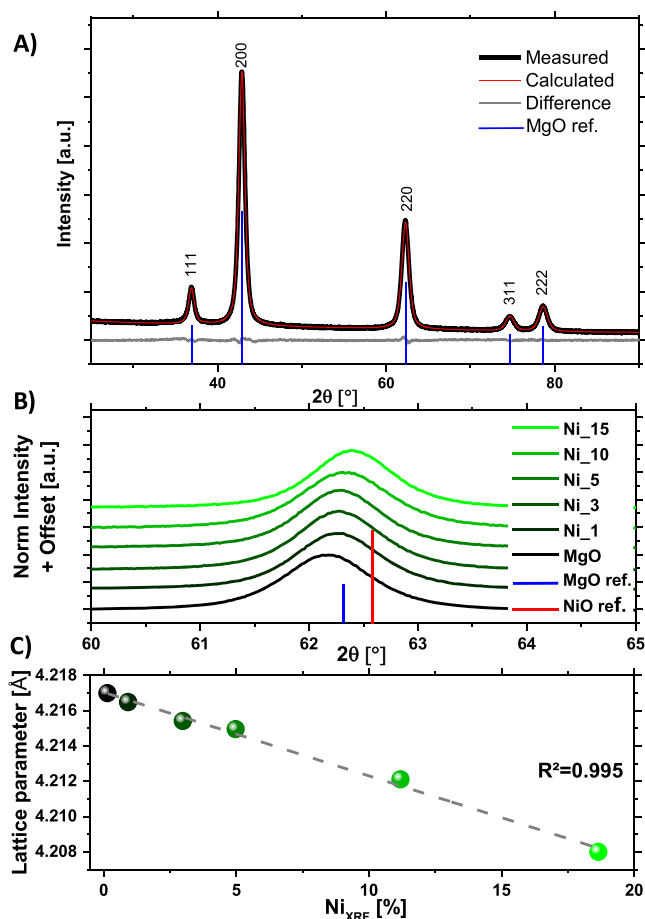
Figure 1. (A) Rietveld fit of Ni_10 with the measured (black line) calculated (red line) diffraction patterns and the corresponding difference curve (gray line). (B) Superposition of the six XRD patterns, zoom in the 60−65° region. (C) Variation of the lattice parameter *a* versus the Ni content determined by XRF.

These findings are in line with the TPR profiles of the catalysts (Figure S7A). Since electron microscopy investigations are not representative of the entire sample, a more integral method was needed to confirm the dispersion of the Ni species inside the MgO structure. The absence of a low temperature reduction event at about 350 °C, indicative for surface agglomerates, and only one strong signal at 750 °C, indicative for Ni atoms embedded in the MgO structure,[29] underline the homogeneous character of the $Ni_xMg_{1-x}O$ solid solution and the absence of NiO agglomerates at the surface.

3.3. Elemental Composition. The global elemental composition (surface + bulk) was determined using X-ray fluorescence (XRF). The experimental values show good agreement with the nominal ones (Table 1). According to a

Table 1. Chemical Constitution of Prepared Catalysts

| ID	Ni% (nominal)	Ni% (XRF)	Ni% (XPS)	FHI database
MgO	0	0	0	#25453
Ni_1	1	0.95	1.96	#23134
Ni_3	3	3.01	5.66	#25477
Ni_5	5	5.01	9.18	#27537
Ni_10	10	11.2	15.25	#23659
Ni_15	15	18.7	24.5	#23769

previous study, the most favorable position for a formal Mg^{2+} substitution by Ni^{2+} ions in a MgO structure is on its corners, coordinatively unsaturated.[24] To investigate the Ni distribution in the structure, X-ray photoemission spectroscopy (XPS) was applied (Figure 3A, Ni 2p(3/2) core levels, Figure S9 Mg 2p spectra). The more surface sensitive XPS analysis reveals a strong surface enrichment by a factor of 2 for Ni in the solid solutions (Figure 3B, Table 1). The obtained spectra of Ni 2p (870−850 eV) show that only Ni^{2+} species are present over the whole range of concentration (Figure 3A). Contrarily to the study of pure NiO, the presented Ni 2p XPS spectra did not show any peak splitting expected at 854−858 eV. The main Ni 2p peak at 854 eV in NiO, which is missing in our spectra, was identified in the literature as characteristic of Ni with neighboring Ni species.[30] Its absence in this study is in line with the high dispersion of the Ni atoms in the MgO structure. A comparison of the surface composition vs the global composition (Ni_{XPS} as a function of Ni_{XRF}) (Figure 3B) shows that from Ni_10 the surface composition is not evolving
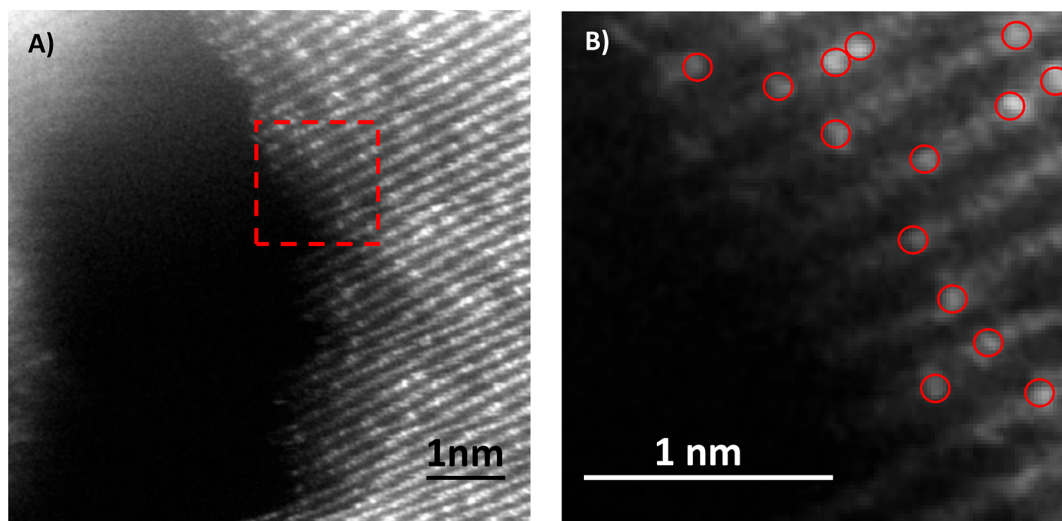
Figure 2. (A) STEM-HAADF image of Ni_10 before catalytic testing. (B) Magnification of the selected area. To guide the eye, some of the brighter spots are circled in red.
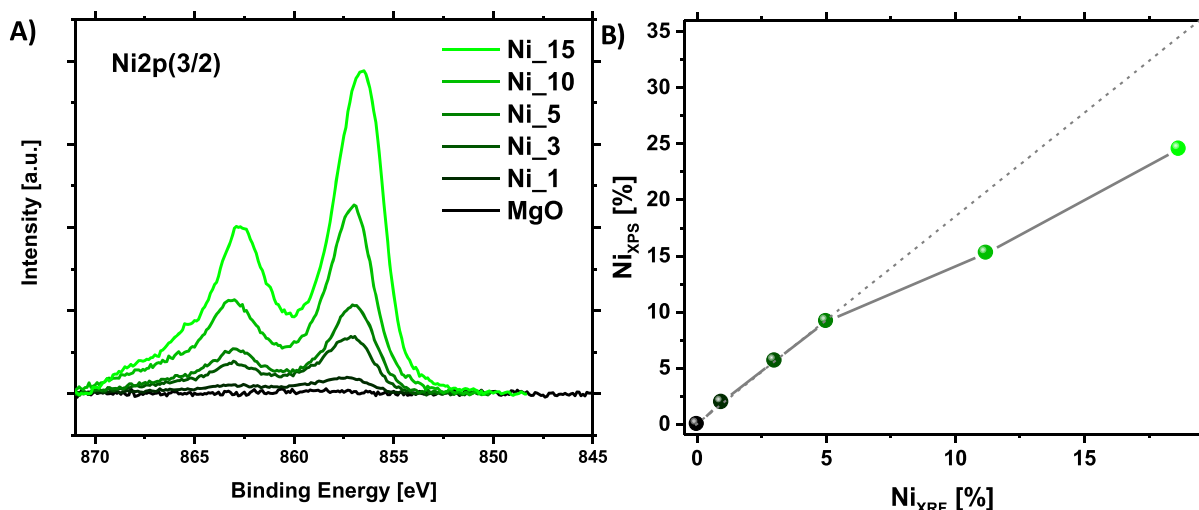
Figure 3. (A) Ni 2p 3/2 spectra in the 870−845 eV region. (B) Surface Ni concentration (measured by XPS) evolution versus the global Ni concentration (measured by XRF).
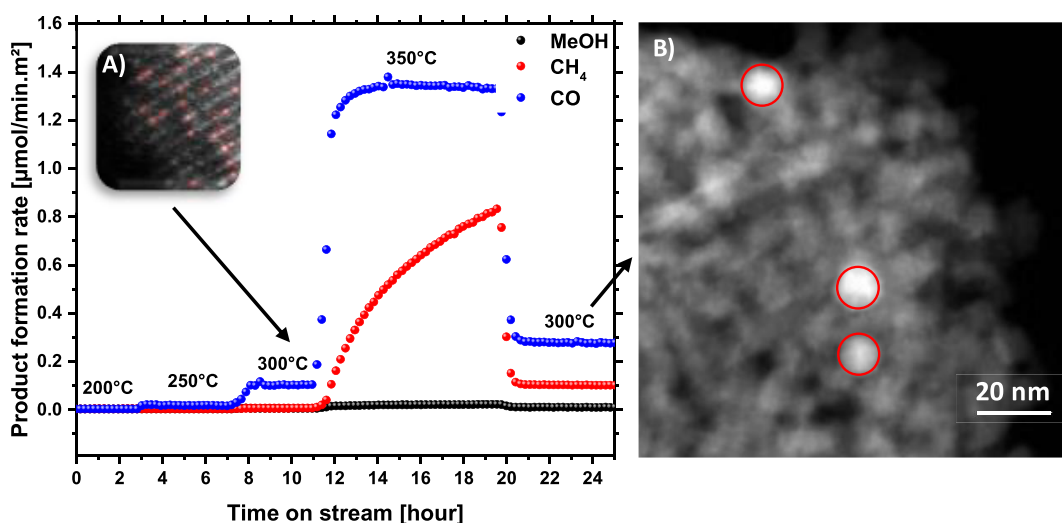
Figure 4. (A) Product formation rate of Ni_10 at 30 bar, different temperatures, upper corner left represent the sample after 300 °C testing (Figure 7). (B) TEM image of the sample after testing at 350 °C.

linearly. A surface saturation phenomenon is indicated for Ni_10 and Ni_15, resulting in a poorer surface Ni concentration (compared to their global Ni content) when compared to the samples with lower Ni loadings (Ni_1, Ni_3, and Ni_5).

As XPS measurements also gain information from the subsurface layers, another merely surface-sensitive technique has to be applied. Microcalorimetry allows us to chemically titrate the surface of the catalysts with CO_2 as probe molecule. The qualitative (differential heat of adsorption) and quantitative (amount of adsorbed molecules until saturation) information extracted from these measurements are shown in Figure S10. A linear correlation is obtained when comparing the amount of CO_2 adsorbed, measured by microcalorimetry, and the Ni concentration obtained by XPS (see Figure 5A). This is strong evidence that the Ni content gained by XPS correlates well with the Ni concentration on the surface of the catalysts. The linear dependency implies again a saturation effect for the Ni_10 sample (see also Figure S11A, amount of CO_2 titrated vs XRF).

3.4. Catalytic Testing. The catalysts were tested at 30 bar, between 200 and 300 °C, and in a gas mixture of H_2/CO_2 of 4:1 (for details see the experimental details). The H_2/CO_2 ratio, the low temperatures, and the elevated pressure were chosen in order to favor the formation of CH_4 over CO, since this selectivity information serves as descriptor for multi-electron reactions. In order to study the reactivity of the isolated Ni atoms, the temperature of 300 °C was not exceeded, as testing at higher temperatures (350 °C) resulted in the formation of Ni clusters of about 10 nm (Figure 4B). Parallel to the Ni cluster formation, the reaction rate of the byproduct CH_4 increased as illustrated in Figure 4A. Details of the EDX mapping are presented Figure S12. Interestingly, at 350 °C MeOH formation was recorded as a rather nontypical product of Ni catalysts. This might be explained by the intermediate character of the Ni cluster, more active than an atom but not yet a metallic particle with respect to, e.g., its oxophilicity[31] or the ability to activate H_2. An ongoing formation of Ni clusters was suppressed as soon as we adjusted the temperature back to 300 °C. Besides CH_4 as the reaction

product, a much higher reaction rate of CO was detected due to the already formed Ni clusters.

The Ni_15 sample already showed CH_4 formation at 300 °C and a large increase of the CO formation rate, similar to what is observed for the testing of Ni_10 at 350 °C (Figure S13 and Figure 4). As the cluster formation and the development of CH_4 as a byproduct appear to be directly related, it is very likely that Ni clusters were already formed at the comparably low temperatures of 300 °C in Ni_15 (sample with the highest Ni concentration). To ensure the reproducibility and to prove that no cluster formation occurred at 300 °C, all samples were tested following an increasing and then decreasing temperature profile (Figure S14). At 300 °C, the catalysts were all 100% selective toward CO. During the testing period of 8 h, no deactivation was observed. Figure 5B shows the CO formation
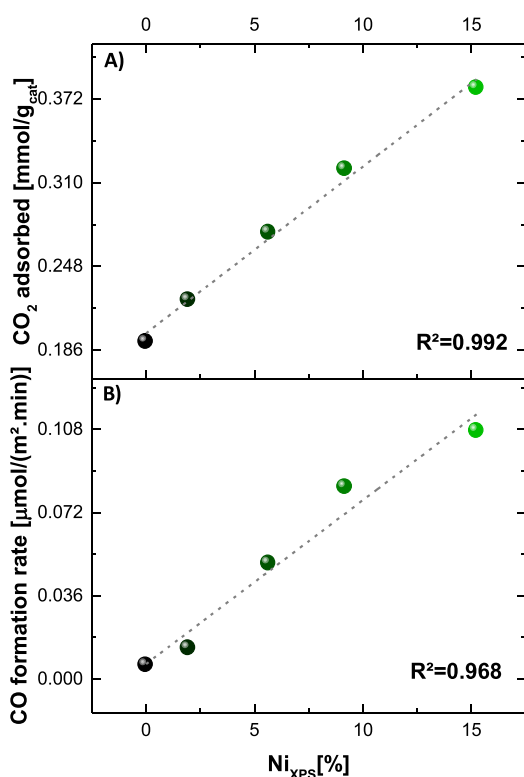
Figure 5. (A) Evolution of the amount of CO_2 adsorbed (measured by microcalorimetry) versus the surface nickel concentration (measured by XPS). (B) Evolution of the CO formation rate as a function of the surface nickel concentration (measured by XPS).

rate (rWGS reaction) as a function of the Ni content determined by XPS and as evidenced above (see also Figure 5A) the Ni concentration on the surface. Since the CO formation rate correlates linearly with the Ni concentration on the surface, it is very likely that the Ni single atoms are directly involved in the catalytic cycle. Due to the discrepancy with XRF results (saturation phenomenon, Figure S11B), the Ni atoms situated in the bulk do not significantly contribute to the observed reactivity. This interpretation is in accordance with theory calculations, which show a negligible impact of Ni in subsurface region for CO_2 and H_2 adsorption (Table 2 and details in Table S8) when compared to Ni atoms on the surface of the oxide. For example, according to theoretical calculations, the adsorption energies; i.e., for CO_2 on terraces are between 62 and 68 kJ mol^{-1} for Ni free and Ni in the first or second subsurface layer of MgO (Figure 6). The small but noticeable increase of CO_2 adsorption energy in the case of MgO (001) surface with Ni in the second atomic layer is explained by additional bonding of $CO_3^{\delta-}$ (including the surface oxygen) with Ni d-states. As the Ni is located deeper in subsurface, the contribution of Ni states to the bonding is decreased.

To gain further information about the stability of these catalysts, selected samples (Ni_3 and Ni_10) were tested over a period of 100 h TOS (Figure S15A,B). Stable CO formation and the absence of CH_4 as a byproduct were observed, which implies indirectly the absence of any cluster formation (as the cluster formation in our study was always accompanied by the development of CH_4 as byproduct).

3.5. Characterization after Catalysis. After catalysis, the samples were thoroughly characterized (after 40 and 100 h TOS) with STEM, TPR, XRD, and TG-MS. Figure 7A (and 7B as zoom-in) shows the STEM investigation of the Ni_10 catalyst after 40 h TOS. The analysis did not reveal the presence of any Ni particles or clusters as only single atoms of Ni in the MgO cubic structure were visible. The stable and selective catalytic performance is in agreement with the absence of Ni particles. To confirm this with a more integral method on a larger scale, XRD Rietveld analysis was performed after catalysis (100 h TOS, Ni_10). Figure 7C shows the absence of any new phases (hydroxides or carbonates) showing the absence of bulk transformation processes upon catalysis, again in line with the high stability of the catalysts even at elevated TOS. Furthermore, the lattice parameter a and the size of the coherent crystalline domains remained unchanged upon catalysis even after 100 h TOS (variations smaller than 3 esd: $a_{before} = 4.21126(7)$ vs $a_{after} = 4.21104(7)$; L_{Vol} _ -IB$_{before}$ = 9.42(12) vs L_{Vol} − IB$_{after}$ = 9.10(14)).

TPR investigations after catalysis (40 h TOS, Ni_10) revealed a specific reduction event at 350 °C, which, however, could not be attributed to the reduction of NiO aggregates,[29] as illustrated in Figures S7 and S8, but to CO and CH_4 formation by hydrogenation of surface species. This confirms again that the testing at 300 °C for extended TOS did not lead to the formation of Ni particles. Furthermore, this experiment

Table 2. Calculation of the Adsorption Energy of CO_2 and of the Dissociative Adsorption of H_2 for Different Sites

	adsorption energy (kJ/mol)					
	CO_2			H_2 (dissociative adsorption)		
adsorption site	terraces	corners	steps	terraces	corners	steps
NiMgO	−61.8	−160.2	−219.0	+109.0	−83.9	−98.4
MgO	−61.8	−199.7	−245.1	+171.7	−48.2	−51.1
MgO (Ni first sublayer)	−67.5	−193.0	−236.4	+171.7	−47.3	−50.2
MgO (Ni second sublayer)	−62.7					

E_{ads}=-61.8kJ/mol E_{ads}=-67.5kJ/mol E_{ads}=-62.7kJ/mol
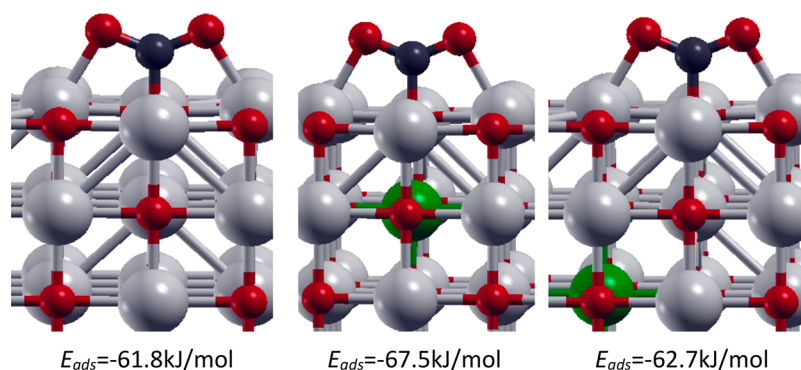
Figure 6. Example of the influence of the adsorption site on the CO_2 adsorption energy for terrace sites. Green represents the Ni which substitutes one of the gray Mg atoms in the first and second subsurface layer. Oxygen is shown in red and carbon in black.
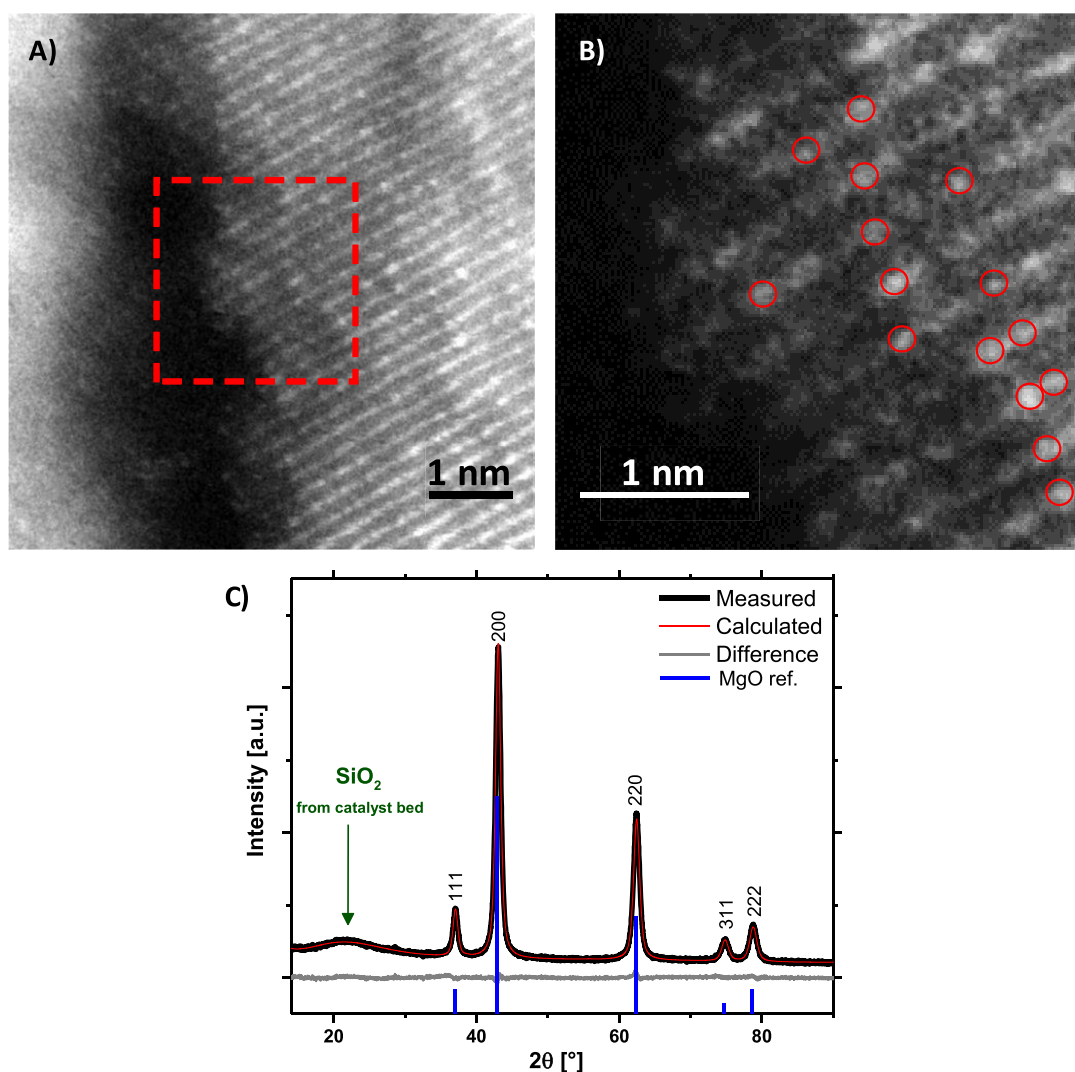
Figure 7. (A) STEM-HAADF image of Ni_10 after catalysis. (B) STEM-HAADF image zoom of the indicated area. To guide the eye, some of the brighter spots are circled in red. (C) Rietveld fit of Ni_10 after 100h time on stream without deactivation, with the measured (black line) calculated (red line) diffraction patterns and the corresponding difference curve (blue line).

reveals that carbonate-based species on the surface of the catalysts are present after reaction.

TG-MS analysis before and after catalysis revealed a clear surface modification upon testing. The thermal decomposition experiments showed a large release of CO_2 at 300 °C that was not observed on the fresh catalyst, together with an additional water release, indicating that the in situ surface modification likely corresponds to the formation of hydrogenated carbonate species (Figure S16).

Considering the amount of CO_2 released (measured by integration of the mass spectrometry signal recorded upon thermal decomposition) and a homogeneous distribution of

the adsorbates on the available BET surface area, a coverage of approximately one monolayer is calculated (Table S4). As expected, XRD was unable to resolve amorphous surface modifications including surface carbonates.

This overlayer formation appear to be closely linked with the stability of the SAC. While testing at 30 bar leads to the stable formation of CO (Figure 5A and Figure S14), the testing at 1 bar leads to the formation of CH_4, which suggests the formation of Ni clusters and particles at already 300 °C, as shown in Figure S17A,B. We observe that with ongoing TOS the selectivity toward CH_4 and the reaction rates increase, in line with the catalyst behavior at 30 bar and 350 °C (Figure 4 and Figure S17B). However, testing at 1 bar after testing at 30 bar leads to stable production of CO with 100% selectivity. The absence of CH_4 as a byproduct consequently evidence the stability of the catalyst without the formation of any Ni clusters (Figure S18). A reconstruction of the catalysts surface has thus taken place in situ at 30 bar. The stability of this surface modification ($\leq$1 ML as shown Table S4), formed at elevated pressures, seems to be directly related to the stability of the Ni atoms, as the agglomeration of Ni is observed in its absence.

This is in good agreement with the results of the in situ IR analysis shown Figure 8A−C (see Table S5 for the assignment
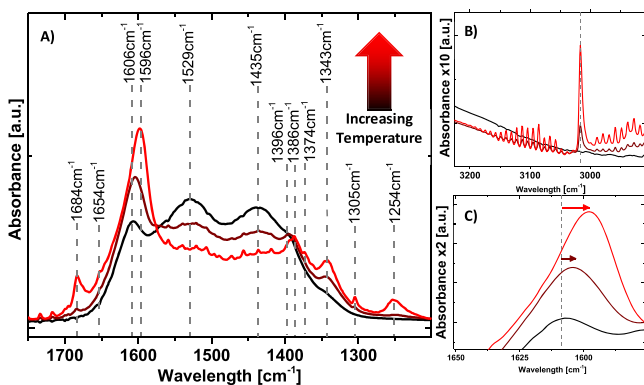
Figure 8. IR spectroscopy under reaction conditions ($4H_2/CO_2$), stepwise increase from 200 °C (black), to 250 °C (dark red), to 300 °C (red): (A) zoom in the 1200−1700 cm^{-1} area; (B) zoom on the 2900−3200 cm^{-1} area; (C) zoom on the 1550−1650 cm^{-1} area.

of the IR modes). At the surface of the catalysts was observed a mixture of different carbonates and hydrogenated carbonates species. With increasing temperature, a progressive decrease of the carbonate signals (1435, 1529 cm^{-1}) from the decomposition of the surface overlayer is observed. This process is accompanied by an increase of the bicarbonate signal (1250 cm^{-1}), formate signals (1342, 1606 cm^{-1}), and the appearance of CH_4 (Figure 8A, 1305 cm^{-1}; Figure 8B, 3016 cm^{-1}). This findings evidence once again the concerted fashion of a CO_2 release due to a progressive instability of the surface overlayer, the agglomeration of the Ni and the formation of CH_4, respectively. Besides, a pronounced shift in the formate area from 1607 to 1596 cm^{-1} is observed, as shown in more detail in Figure 8C. While values around 1600−1606 cm^{-1} were attributed to formates species on MgO,[32] values around 1591 cm^{-1} were recently reported for stretching vibrations from formate species on Ni^0 nanoclusters,[14] further supporting the correlation of cluster formation and CH_4 production. The same shift was observed in the formate C−H area (∼2900 cm^{-1}) as seen Figure S19. The stepwise red-shift of the

formate stretching vibration with the formation of Ni clusters might be interpreted as a weakening of the conjugated C−O/C=O system on Ni clusters or at the metal/metal oxide interface, consequently visible in its increased catalytic performance (increasing CH_4 rates).

3.6. Final Discussion. *Microcalorimetry.* Theoretical calculations (Table 2) predict for the adsorption of CO_2 three main types of sites: low energy sites (terraces −61.8 kJ mol^{-1}), intermediate energy sites (corners −160.2/−199.7 kJ mol^{-1}), and high energy sites (steps −219.0/−245.1 kJ mol^{-1}). Comparing the qualitative analysis of the catalysts (Figure S10) in terms of their differential heats of adsorption, almost similar values are obtained (between 105 and 125 kJ mol^{-1} for all samples). These energies could be attributed to the intermediary energy sites (corners), as under a mild vacuum pretreatment, the high energy sites (steps) are not accessible (as seen by CO adsorption IR at 77K Figure S20 and Table S6).

The discrepancy observed between the theoretical values and the experimental ones could be explained, by the "uniform roughness" of the catalysts surface, the dependency of the E_{ads} on the CO_2 coverage[33] and by the Ni content (Tables S7 and S8) that tends to lower the adsorption energies.

The increase of the CO_2 uptake with the Ni concentration indicates that also the amount of available sites for titration (mainly corners) increased. This is in good agreement with the theoretical predictions suggesting that the most favorable position for a Ni^{2+} substitution is at the low coordinated sites (corners and steps) of the MgO. Further, the incorporation of Ni inside the structure might cause morphological changes, increasing the amount of corners in the structure, in order to allow the Ni atoms to reach their thermodynamically most favored position. The roughened surface rich in corners/steps is directly evidenced by overview TEM images (Figure S21), which is in agreement with the presence of Ni on unsaturated sites.

Catalysis. We observe a linear evolution of the reactivity with the Ni surface concentration, clearly indicating that the Ni surface sites are involved in the catalytic cycle, while their isolation and the absence of agglomeration explains the linear character of the correlation. Under reaction conditions, a surface adsorbate layer was formed (carbonate-based species). The stability of this reactant induced restructuring is directly linked with the stability of the catalysts and their high selectivity toward CO. The involvement of the surface Ni atoms in the catalytic cycle could be related to the poorer stability of carbonate-based intermediates on Ni sites, in accordance with the calculated adsorption energy of CO_2 on Ni vs Mg (Table2, S,S). Ni would promote the formation of "CO_2 vacancies" in this carbonate layer and enable the activation of H_2 molecules leading to their catalytic dissociation. Indeed, to conduct the rWGS reaction, it is crucial to adsorb and dissociate the H_2 molecules, a process which is much more favorable on Ni atoms as part of the MgO instead of pure MgO. That means Ni changes the surface termination and population of corners and steps of the entire catalysts since coordinatively unsaturated sites are thermodynamically favored.[24] Besides this structural impact, Ni has a direct influence on the reactants, increasing the activation of H_2 and decreasing the stability of activated CO_2 accessible for its catalytic conversion.

Particle Formation. While the isolated Ni atoms were active for the activation of CO_2, their selectivity was restricted to CO,

and the formation of Ni clusters (even of a few nm) was necessary to form higher value-added products such as CH_4[14] or even MeOH. Indeed, the single atoms are only able to take part in the $2e^-$ redox cycle, while to perform the full hydrogenation of CO_2 (the $8e^-$ redox cycle), Ni clusters are crucial. Furthermore, the product formation rates increased by a factor of 3 at the same temperatures after particle formation occurred (Figure 4).

4. CONCLUSIONS

Through the synthesis of phase pure precursors and catalysts, we prepared for the first time Ni single atom catalysts using wet chemistry. Ni concentrations of up to 10 atom % were achieved and identified as the upper limit for the function of single atom catalyst. The anchoring of the Ni and its stabilization was achieved by a solid solution approach. A Ni surface enrichment of the solid solutions is observed, by both physical and chemical analysis methods, in agreement with the prediction made from first principle calculations.[24] This enrichment somehow has its restrictions, as samples containing 10 atom % Ni or more show a saturation phenomenon. These Ni single atom catalysts are active for CO_2 activation in the reverse-water–gas-shift reaction. A stable performance over time, which evolved linearly with the amount of Ni on the surface, is observed. We exclude that the dominant effect of this reactivity is a bulk effect. Further, we show that the main contribution is originated from the amount of Ni atoms on the surface of the catalysts. During catalysis, a carbonate-based overlayer was formed, and its decomposition appears to be coupled to the Ni agglomeration. Finally, isolated Ni atoms were not able to hydrogenate CO_2 to higher value added products such as CH_4 or MeOH, for which Ni clusters are necessary. The simplification of the size of active sites toward single atoms seems to have limitations, since the ability to catalyze a multielectron reaction is attributed to at least Ni clusters. The selectivity change toward CH_4 and the progressive increase of the reaction rates (CO and CH_4) for the samples with Ni clusters give insight into the different reactivity regimes occurring before and after the particle formation. The reactant-induced surface overlayer mechanism for the Ni single atom catalysts is consecutively substituted by a formate-based one, in which the continuously growing Ni clusters/particles decrease the formate stability. This leads to higher reaction rates and higher CH_4 selectivities. Within this $Ni_xMg_{1-x}O$ solid solution study we bridge for the first time the Ni single atom to Ni cluster regime as an example of the limited applicability of SACs as high performance catalysts. In addition, this fundamental contribution to the mechanistic understanding in the development of catalytic selectivity and activity serves as new approach adaptable to other reactions and systems forming solid solutions.

ASSOCIATED CONTENT

Ⓢ Supporting Information

The Supporting Information is available free of charge on the ACS Publications website at DOI: 10.1021/jacs.8b11729.

> Synthesis protocol, details of all powder X-ray diffraction measurements, electron microscopy, microcalorimetry, details of the catalytic testing, details of the thermal analysis, IR spectroscopy, and theoretical calculations (PDF)

AUTHOR INFORMATION

Corresponding Author

*efrei@fhi-berlin.mpg.de

ORCID Ⓞ

Aliaksei Mazheika: 0000-0002-4705-1804

Elias Frei: 0000-0003-3565-1199

Notes

The authors declare no competing financial interest.

REFERENCES

(1) Yang, X.-F.; Wang, A.; Qiao, B.; Li, J.; Liu, J.; Zhang, T. Single-Atom Catalysts: A New Frontier in Heterogeneous Catalysis. *Acc. Chem. Res.* **2013**, *46* (8), 1740−1748.

(2) (a) Herzing, A. A.; Kiely, C. J.; Carley, A. F.; Landon, P.; Hutchings, G. J. Identification of Active Gold Nanoclusters on Iron Oxide Supports for CO Oxidation. *Science* **2008**, *321* (5894), 1331−1335. (b) Turner, M.; Golovko, V. B.; Vaughan, O. P. H.; Abdulkin, P.; Berenguer-Murcia, A.; Tikhov, M. S.; Johnson, B. F. G.; Lambert, R. M. Selective oxidation with dioxygen by gold nanoparticle catalysts derived from 55-atom clusters. *Nature* **2008**, *454* (7207), 981−983. (c) Molina, L. M.; Lee, S.; Sell, K.; Barcaro, G.; Fortunelli, A.; Lee, B.; Seifert, S.; Winans, R. E.; Elam, J. W.; Pellin, M. J.; Barke, I.; von Oeynhausen, V.; Lei, Y.; Meyer, R. J.; Alonso, J. A.; Fraile Rodríguez, A.; Kleibert, A.; Giorgio, S.; Henry, C. R.; Meiwes-Broer, K.-H.; Vajda, S. Size-dependent selectivity and activity of silver nanoclusters in the partial oxidation of propylene to propylene oxide and acrolein: A joint experimental and theoretical study. *Catal. Today* **2011**, *160* (1), 116−130. (d) Zhang, X.; Shi, H.; Xu, B.-Q. Catalysis by Gold: Isolated Surface Au3+ Ions are Active Sites for Selective Hydrogenation of 1,3-Butadiene over Au/ZrO2 Catalysts. *Angew. Chem., Int. Ed.* **2005**, *44* (43), 7132−7135. (e) Qiao, B.; Wang, A.; Yang, X.; Allard, L. F.; Jiang, Z.; Cui, Y.; Liu, J.; Li, J.; Zhang, T. Single-atom catalysis of CO oxidation using Pt1/FeOx. *Nat. Chem.* **2011**, *3* (8), 634−641. (f) Murzin, D. Y. On Cluster Size Dependent Activity and Selectivity in Heterogeneous Catalysis. *Catal. Lett.* **2012**, *142* (11), 1279−1285. (g) Rioux, R. M.; Hsu, B. B.; Grass, M. E.; Song, H.; Somorjai, G. A. Influence of Particle Size on Reaction Selectivity in Cyclohexene Hydrogenation and Dehydrogenation over Silica-Supported Monodisperse Pt Particles. *Catal. Lett.* **2008**, *126* (1−2), 10. (h) Kuhn, J. N.; Huang, W.; Tsung, C.-K.; Zhang, Y.; Somorjai, G. A. Structure Sensitivity of Carbon−Nitrogen Ring Opening: Impact of Platinum Particle Size from below 1 to 5 nm upon Pyrrole Hydrogenation Product Selectivity over Monodisperse Platinum Nanoparticles Loaded onto Mesoporous Silica. *J. Am. Chem. Soc.* **2008**, *130* (43), 14026−14027.

(3) Thomas, J. M. How Far is the Concept of Isolated Active Sites Valid in Solid Catalysts? *Top. Catal.* **2008**, *50* (1−4), 98−105.

(4) (a) Callahan, J. L.; Grasselli, R. K. A selectivity factor in vapor-phase hydrocarbon oxidation catalysis. *AIChE J.* **1963**, *9* (6), 755−760. (b) Grasselli, R. K.; Buttrey, D. J.; DeSanto, P., Jr; Burrington, J. D.; Lugmair, C. G.; Volpe, A. F., Jr; Weingand, T. Active centers in

Mo−V−Nb−Te−Ox (amm)oxidation catalysts. *Catal. Today* **2004**, *91−92*, 251−258. (c) Grasselli, R. K. Fundamental Principles of Selective Heterogeneous Oxidation Catalysis. *Top. Catal.* **2002**, *21* (1−3), 79−88.

(5) (a) Gu, X.-K.; Qiao, B.; Huang, C.-Q.; Ding, W.-C.; Sun, K.; Zhan, E.; Zhang, T.; Liu, J.; Li, W.-X. Supported Single Pt1/Au1 Atoms for Methanol Steam Reforming. *ACS Catal.* **2014**, *4* (11), 3886−3890. (b) Nie, L.; Mei, D.; Xiong, H.; Peng, B.; Ren, Z.; Hernandez, X. I. P.; DeLaRiva, A.; Wang, M.; Engelhard, M. H.; Kovarik, L.; Datye, A. K.; Wang, Y. Activation of surface lattice oxygen in single-atom Pt/CeO2 for low-temperature CO oxidation. *Science* **2017**, *358* (6369), 1419−1423.

(6) Qiao, B.; Liang, J.-X.; Wang, A.; Xu, C.-Q.; Li, J.; Zhang, T.; Liu, J. J. Ultrastable single-atom gold catalysts with strong covalent metal-support interaction (CMSI). *Nano Res.* **2015**, *8* (9), 2913−2924.

(7) (a) Liang, J.-X.; Lin, J.; Yang, X.-F.; Wang, A.-Q.; Qiao, B.-T.; Liu, J.; Zhang, T.; Li, J. Theoretical and Experimental Investigations on Single-Atom Catalysis: Ir1/FeOx for CO Oxidation. *J. Phys. Chem. C* **2014**, *118* (38), 21945−21951. (b) Lin, J.; Wang, A.; Qiao, B.; Liu, X.; Yang, X.; Wang, X.; Liang, J.; Li, J.; Liu, J.; Zhang, T. Remarkable Performance of Ir1/FeOx Single-Atom Catalyst in Water Gas Shift Reaction. *J. Am. Chem. Soc.* **2013**, *135* (41), 15314−15317.

(8) Aich, P.; Wei, H.; Basan, B.; Kropf, A. J.; Schweitzer, N. M.; Marshall, C. L.; Miller, J. T.; Meyer, R. Single-Atom Alloy Pd−Ag Catalyst for Selective Hydrogenation of Acrolein - The. *J. Phys. Chem. C* **2015**, *119* (32), 18140.

(9) (a) Silaghi, M.-C.; Comas-Vives, A.; Copéret, C. CO2 Activation on Ni/γ−Al2O3 Catalysts by First-Principles Calculations: From Ideal Surfaces to Supported Nanoparticles. *ACS Catal.* **2016**, *6* (7), 4501−4505. (b) Lin, W.; Stocker, K. M.; Schatz, G. C. Mechanisms of Hydrogen-Assisted CO2 Reduction on Nickel. *J. Am. Chem. Soc.* **2017**, *139* (13), 4663−4666. (c) Heine, C.; Lechner, B. A. J.; Bluhm, H.; Salmeron, M. Recycling of CO2: Probing the Chemical State of the Ni(111) Surface during the Methanation Reaction with Ambient-Pressure X-Ray Photoelectron Spectroscopy. *J. Am. Chem. Soc.* **2016**, *138* (40), 13246−13252. (d) Roiaz, M.; Monachino, E.; Dri, C.; Greiner, M.; Knop-Gericke, A.; Schlögl, R.; Comelli, G.; Vesselli, E. Reverse Water−Gas Shift or Sabatier Methanation on Ni(110)? Stable Surface Species at Near-Ambient Pressure. *J. Am. Chem. Soc.* **2016**, *138* (12), 4146−4154.

(10) Garbarino, G.; Riani, P.; Magistri, L.; Busca, G. A study of the methanation of carbon dioxide on Ni/Al2O3 catalysts at atmospheric pressure. *Int. J. Hydrogen Energy* **2014**, *39* (22), 11557−11565.

(11) (a) Mette, K.; Kühl, S.; Düdder, H.; Kähler, K.; Tarasov, A.; Muhler, M.; Behrens, M. Stable Performance of Ni Catalysts in the Dry Reforming of Methane at High Temperatures for the Efficient Conversion of CO2 into Syngas. *ChemCatChem* **2014**, *6* (1), 100−104. (b) Tomishige, K. Syngas production from methane reforming with CO2/H2O and O2 over NiO−MgO solid solution catalyst in fluidized bed reactors. *Catal. Today* **2004**, *89* (4), 405−418. (c) Zuo, Z.; Liu, S.; Wang, Z.; Liu, C.; Huang, W.; Huang, J.; Liu, P. Dry Reforming of Methane on Single-Site Ni/MgO Catalysts: Importance of Site Confinement. *ACS Catal.* **2018**, *8* (10), 9821−9835.

(12) Wu, H. C.; Chang, Y. C.; Wu, J. H.; Lin, J. H.; Lin, I. K.; Chen, C. S. Methanation of CO2 and reverse water gas shift reactions on Ni/SiO2 catalysts: the influence of particle size on selectivity and reaction pathway. *Catal. Sci. Technol.* **2015**, *5* (8), 4154−4163.

(13) (a) Lu, B.; Kawamoto, K. Preparation of mesoporous CeO2 and monodispersed NiO particles in CeO2, and enhanced selectivity of NiO/CeO2 for reverse water gas shift reaction. *Mater. Res. Bull.* **2014**, *53*, 70−78. (b) Chen, C.-S.; Budi, C. S.; Wu, H.-C.; Saikia, D.; Kao, H.-M. Size-Tunable Ni Nanoparticles Supported on Surface-Modified, Cage-Type Mesoporous Silica as Highly Active Catalysts for CO2 Hydrogenation. *ACS Catal.* **2017**, *7* (12), 8367−8381.

(14) Vogt, C.; Groeneveld, E.; Kamsma, G.; Nachtegaal, M.; Lu, L.; Kiely, C. J.; Berben, P. H.; Meirer, F.; Weckhuysen, B. M. Unravelling structure sensitivity in CO 2 hydrogenation over nickel. *Nature Catalysis* **2018**, *1* (2), 127−134.

(15) (a) Qiu, H. J.; Ito, Y.; Cong, W.; Tan, Y.; Liu, P.; Hirata, A.; Fujita, T.; Tang, Z.; Chen, M. Nanoporous Graphene with Single-Atom Nickel Dopants: An Efficient and Stable Catalyst for Electrochemical Hydrogen Production. *Angew. Chem., Int. Ed.* **2015**, *54* (47), 14031−14035. (b) Zhao, C.; Dai, X.; Yao, T.; Chen, W.; Wang, X.; Wang, J.; Yang, J.; Wei, S.; Wu, Y.; Li, Y. Ionic Exchange of Metal−Organic Frameworks to Access Single Nickel Sites for Efficient Electroreduction of CO2. *J. Am. Chem. Soc.* **2017**, *139* (24), 8078−8081. (c) Fei, H.; Dong, J.; Feng, Y.; Allen, C. S.; Wan, C.; Volosskiy, B.; Li, M.; Zhao, Z.; Wang, Y.; Sun, H.; An, P.; Chen, W.; Guo, Z.; Lee, C.; Chen, D.; Shakir, I.; Liu, M.; Hu, T.; Li, Y.; Kirkland, A. I.; Duan, X.; Huang, Y. General synthesis and definitive structural identification of MN 4 C 4 single-atom catalysts with tunable electrocatalytic activities. *Nature Catalysis* **2018**, *1* (1), 63−72.

(16) Gonçalves, R. V.; Vono, L. L. R.; Wojcieszak, R.; Dias, C. S. B.; Wender, H.; Teixeira-Neto, E.; Rossi, L. M. Selective hydrogenation of CO2 into CO on a highly dispersed nickel catalyst obtained by magnetron sputtering deposition: A step towards liquid fuels. *Appl. Catal., B* **2017**, *209*, 240−246.

(17) (a) Kuzmin, A.; Mironova, N. Composition dependence of the lattice parameter in NicMg1-cO solid solutions. *J. Phys.: Condens. Matter* **1998**, *10* (36), 7937−7944. (b) Kuzmin, A.; Mironova, N.; Purans, J.; Rodionov, A. X-ray absorption spectroscopy study of NicMg1-cO solid solutions on the Ni K edge. *J. Phys.: Condens. Matter* **1995**, *7* (48), 9357−9368.

(18) (a) Tomishige, K.; Yamazaki, O.; Chen, Y.; Yokoyama, K.; Li, X.; Fujimoto, K. Development of ultra-stable Ni catalysts for CO2 reforming of methane. *Catal. Today* **1998**, *45* (1−4), 35−39. (b) Hu, Y. H. Solid-solution catalysts for CO2 reforming of methane. *Catal. Today* **2009**, *148* (3−4), 206−211. (c) Carreiro, J. A. S. P.; Baerns, M. Oxidative coupling of methane. *J. Catal.* **1989**, *117* (1), 258−265.

(19) McClellan, A. L.; Harnsberger, H. F. Cross-sectional areas of molecules adsorbed on solid surfaces. *J. Colloid Interface Sci.* **1967**, *23* (4), 577−599.

(20) Yeh, J. J.; Lindau, I. Atomic subshell photoionization cross sections and asymmetry parameters: 1 ⩽ Z ⩽ 103. *At. Data Nucl. Data Tables* **1985**, *32* (1), 1−155.

(21) Brunauer, S.; Emmett, P. H.; Teller, E. Adsorption of Gases in Multimolecular Layers. *J. Am. Chem. Soc.* **1938**, *60*, 309−319.

(22) Farra, R.; Wrabetz, S.; Schuster, M. E.; Stotz, E.; Hamilton, N. G.; Amrute, A. P.; Pérez-Ramírez, J.; López, N.; Teschner, D. Understanding CeO2 as a Deacon catalyst by probe molecule adsorption and in situ infrared characterisations. *Phys. Chem. Chem. Phys.* **2013**, *15* (10), 3454−3465.

(23) Heyd, J.; Scuseria, G. E.; Ernzerhof, M. Hybrid functionals based on a screened Coulomb potential. *J. Chem. Phys.* **2003**, *118* (18), 8207−8215.

(24) Mazheika, A.; Levchenko, S. V. Ni Substitutional Defects in Bulk and at the (001) Surface of MgO from First-Principles Calculations. *J. Phys. Chem. C* **2016**, *120* (47), 26934−26944.

(25) Blum, V.; Gehrke, R.; Hanke, F.; Havu, P.; Havu, V.; Ren, X.; Reuter, K.; Scheffler, M. Ab initio molecular simulations with numeric atom-centered orbitals. *Comput. Phys. Commun.* **2009**, *180* (11), 2175−2196.

(26) Lenthe, E. v.; Baerends, E. J.; Snijders, J. G. Relativistic regular two-component Hamiltonians. *J. Chem. Phys.* **1993**, *99* (6), 4597−4610.

(27) Tkatchenko, A.; DiStasio, R. A.; Car, R.; Scheffler, M. Accurate and Efficient Method for Many-Body van der Waals Interactions. *Phys. Rev. Lett.* **2012**, *108* (23), 236402.

(28) (a) Asencios, Y. J. O.; Bellido, J. D. A.; Assaf, E. M. Synthesis of NiO−MgO−ZrO2 catalysts and their performance in reforming of model biogas. *Appl. Catal., A* **2011**, *397* (1−2), 138−144. (b) Li, Y.; Lu, G.; Ma, J. Highly active and stable nano NiO−MgO catalyst encapsulated by silica with a core−shell structure for CO2 methanation. *RSC Adv.* **2014**, *4* (34), 17420−17428.

(29) (a) Arena, F.; Frusteri, F.; Parmaliana, A.; Giordano, N. On the reduction of NiO forms in magnesia supported catalysts. *React. Kinet. Catal. Lett.* **1990**, *42* (1), 121−126. (b) Jafarbegloo, M.; Tarlani, A.;

Mesbah, A. W.; Muzart, J.; Sahebdelfar, S. NiO−MgO Solid Solution Prepared by Sol−Gel Method as Precursor for Ni/MgO Methane Dry Reforming Catalyst: Effect of Calcination Temperature on Catalytic Performance. *Catal. Lett.* **2016**, *146* (1), 238−248. (c) Parmaliana, A.; Arena, F.; Frusteri, F.; Giordano, N. Temperature-programmed reduction study of NiO−MgO interactions in magnesia-supported Ni catalysts and NiO−MgO physical mixture. *J. Chem. Soc., Faraday Trans.* **1990**, *86* (14), 2663−2669.

(30) Alders, D.; Voogt, F. C.; Hibma, T.; Sawatzky, G. A. Nonlocal screening effects in 2p x-ray photoemission spectroscopy of NiO (100). *Phys. Rev. B: Condens. Matter Mater. Phys.* **1996**, *54* (11), 7716−7719.

(31) Dietz, L.; Piccinin, S.; Maestri, M. Mechanistic Insights into CO_2 Activation via Reverse Water−Gas Shift on Metal Surfaces. *J. Phys. Chem. C* **2015**, *119* (9), 4959−4966.

(32) (a) Busca, G.; Lamotte, J.; Lavalley, J. C.; Lorenzelli, V. FT-IR study of the adsorption and transformation of formaldehyde on oxide surfaces. *J. Am. Chem. Soc.* **1987**, *109* (17), 5197−5202. (b) Busca, G.; Lorenzelli, V. Infrared spectroscopic identification of species arising from reactive adsorption of carbon oxides on metal oxide surfaces. *Mater. Chem.* **1982**, *7* (1), 89−126. (c) Trillo, J. M.; Munuera, G.; Criado, J. M. Catalytic Decomposition of Formic Acid on Metal Oxides. *Catal. Rev.: Sci. Eng.* **1972**, *7* (1), 51−86.

(33) Solis, B. H.; Cui, Y.; Weng, X.; Seifert, J.; Schauermann, S.; Sauer, J.; Shaikhutdinov, S.; Freund, H.-J. Initial stages of CO_2 adsorption on CaO: a combined experimental and computational study. *Phys. Chem. Chem. Phys.* **2017**, *19* (6), 4231−4242.